Research

Author for correspondence:
Saad Bhamla
e-mail: saadb@chbe.gatech.edu

†These authors contributed equally to the study.

THE ROYAL SOCIETY
PUBLISHING

Mastering the Manu—how humans create large splashes

Pankaj Rohilla†, Daehyun Choi†, Halley Wallace†, Kai Lauren Yung†, Juhi Deora, Atharva Lele and Saad Bhamla

Department of Chemical and Biomolecular Engineering, Georgia Institute of Technology, Atlanta, GA, USA

PR, 0000-0002-1918-9902; SB, 0000-0002-9788-9920

Manu jumping, a popular water diving style among Māori people in New Zealand, focuses on creating large splashes. Divers perform aerial manoeuvres such as the 'utkatasana' pose, entering the water in a V-shape, and executing underwater manoeuvres to enhance the splash size. Our study explores the underlying fluid dynamics of Manu jumping and demonstrates how two key parameters, the V-angle and the timing of body opening, can enhance Worthington jet formation. To accurately replicate human Manu jumping, we studied water entry of both passive solid objects with varying V-angles and an active body opening robot (Manubot). The analysis revealed that a 45° V-angle enhances Worthington jet formation, consistent with human diving data. This angle balances a large cavity size and a deep pinch-off depth. The body opening within a timing window of $\hat{t}_r = 1.1-1.5$ synchronizes the robot's potential energies to be timely transferred to the cavity formation, producing the strongest and most vertical, i.e. ideal, Worthington jets. Based on our experimental findings, we propose a range of parameters for generating the large Manu splashes. These insights offer engineering perspectives on how to modulate underwater cavity dynamics using both passive and active body formations.

1. Introduction

Māori Kiwis engage in their beloved traditional water sport called Manu jumping, where participants leap from bridges, docks, waterholes, and diving platforms, aiming to produce the largest possible splashes. For Māori people, Manu jumping is more than just a recreational activity; it is a cultural way of life. Despite their mastery of this art form, the fluid dynamics underlying this unique form of jumping has not yet been studied. Competitions such as the Z Manu World Champs, held across New Zealand, evaluate Manu jumping performances primarily based on the size of the splash created [1]. In Manu jumping, generating a water splash is colloquially known as 'popping a Manu' [2].

The hydrodynamics of Manu jumping is closely related to the water entry of the projectiles. When a projectile impacts a liquid surface, it creates an air cavity in its wake that collapses to produce a liquid jet, known as the Worthington jet [3–7]. The cavity pinch-off forms a base region that feeds and dictates the jet strength [4,8]. The formation of the Worthington jet is driven by the kinetic energy distributed across the collapsing cavity wall, with its acceleration primarily provided by the large vertical momentum around the jet base rather than the pinch-off singularity [8]. While the water entry of solid projectiles and droplets has been extensively studied [9,10], most research has focused on minimizing splash formation, understanding their fluid–structure interaction and small-scale dynamics, and reducing damage to solid projectiles, ships, and seaplanes [3,11–19]. A study focusing on creating large Worthington splashes is still missing.

Prior studies investigating humans and animals diving into water primarily focused on understanding the safety limits and minimizing the splash created by their water entry, as seen in activities like Olympic diving and birds hunting in open waters [20–26]. Additionally, post-entry active movements by divers have been investigated via physical models to minimize splash formation, commonly referred to as a 'rip' entry [25]. Professional water diving takeoff heights can reach up to 27 m [27], with an injury rate of 9.7 injuries per hour of exposure [28]. In comparison, Manu jumping takeoff heights can reach up to 10 m, which can still pose injury risks to both elite athletes and young divers [29,30]. Unlike professional diving, where the focus is on clean, head-first entry, Manu jumping involves participants landing on their backs and glutes, forming a distinctive V-shape at water entry with their bodies.

The key dimensionless numbers governing water entry dynamics of humans and solid projectiles include the Froude number ($Fr = u/\sqrt{gL}$), Bond number ($Bo = \rho g L^2/\sigma$), Weber number ($We = \rho v^2 L/\sigma$) and Reynolds number ($Re = Lu\rho/\mu$); where u is the projectile impact speed on water, L is the characteristic length of the projectile ($L = W$, the width of human jumpers, ρ is water density, μ is the water viscosity, σ is water surface tension, and g is the acceleration due to gravity) [4,5,22]. For human water entry, these numbers typically fall within the ranges $10^4 < Bo < 10^5$, $1 < Fr < 100$, $10^6 < Re < 10^7$, and $10^4 < We < 10^7$. These values indicate that the inertial forces of humans entering the water dominate gravitational, surface tension, and viscous forces, creating an air cavity that collapses via gravitational forces to generate Worthington jets and splashes.

Here, we investigate the fluid dynamics of Manu jumping through human data, and passive and active robotic projectiles. We drop these solid projectiles in water to study the role of jumping height, V-angle during water entry, and the effect of underwater body expansion on the resulting Worthington splash, quantified by its maximum height and maximum projected area. To evaluate the role of human dynamics in popping a big Manu splash, we designed and tested the water entry of solid projectiles with varying V-angles and underwater manoeuvres of an active robot simulating Manu jumpers. Our work offers scientific insights into recreational water jumping sports and underscores the importance of using a V-shape and underwater manoeuvres to create large splashes in water.

2. Methods

2.1. Human data collection

Human Manu jumping data were extracted from 50 YouTube videos. The body dimensions of the jumpers, including height (H) and width (W), were measured using ImageJ. The key parameters such as the jumping height (H_{jump}) and splash height (H_{splash}) were also measured using ImageJ. For human Manu jumping, the maximum splash area could not be accurately measured due to the limited resolution and quality of YouTube videos, which hindered the estimation of the splash area, including satellite droplets. Therefore, we only reported the splash height for human Manu jumping. Moreover, as humans interact with the air cavity along the width-side rather than the lengthwise, and to avoid the scale approximation of human bodies (assumed $h = 1.71$ m), we normalized the jump height and splash height by the body width, resulting in dimensionless jump height ($\beta_{jump} = H_{jump}/W$) and dimensionless splash height ($\beta_{splash} = H_{splash}/W$).

2.2. Solid bodies

Five solid bodies of varying shapes, each with distinct V-angles (0°, 45°, 90°, 120°, and 180°), were designed to mimic the body posture of human Manu jumpers during water entry. These solid bodies were fabricated using a three-dimensional (3D) printer (Bambu Lab X1-Carbon) with polylactic acid (PLA) filament with 100% infill density, ensuring high-density prints for complete submersion in water. The body density and aspect ratio ($W : H$) of the solid bodies were kept constant at 1.24 kg m^{-3} and 1 : 4, respectively. The slamming curvatures at the apex of the solid bodies were kept consistent. A flat-head hex bolt was embedded at the centre of the solid bodies, allowing them to be secured to an electromagnet. The bodies were suspended by the electromagnet at an initial height H_o above water, contained in a water tank of the dimensions $600 \times 400 \times 400$ mm^3 (figure 9 in the appendix A). The Manubot was held using two electromagnets. The solid bodies were released from three different heights (H_o), resulting in three impact speeds, estimated as $u \approx \sqrt{2gH_o}$, ranging from 0.75 to 2 m s^{-1}. The solid projectiles (wedges) were 50 mm in length, with a mass of approximately 5.79 g and a density of approximately 1600 kg m^{-3}.

2.3. Manubot

The Manubot is designed to simulate the underwater opening dynamics of human bodies during the Manu jump, focusing on the initial water entry angle, actuation, and timing of opening. Its 3D-printed body, fabricated using the same method as described for solid bodies earlier, includes a hinge mechanism, enabling it to open actively (mimicking the underwater rollback and kick motion of humans); this mechanism includes a geared motor and the angle restrictor attachments. The angle restrictor prevents the body from closing completely, maintaining a specific angle that can be adjusted by changing the length of the attachment. Figure 6a shows the robot in its closed (top) and open (bottom) positions. The Manubot measures 180 mm in length, with a mass of approximately 115 g and a density of approximately 1300 kg m^{-3}, respectively.

The opening of the robot body is driven by a spring-and-release mechanism, with metal nuts attached to its ends to facilitate its connection with the electromagnet system, ensuring its controlled release during water drop experiments. Inside the body, a geared motor (CL 1.5 Micro Motor) operates the release mechanism, using a thread to control movement. A microprocessor

(Arduino Nano) controls the timing of the release mechanism (t_r = 0.04–0.32 s, where t_r denotes the body opening time), which is powered by the motor. For the no-opening case (when the Manubot never opens), the body opening time is expressed as $t_r \to \infty$.

A simple spring–mass model was used to measure the spring coefficient (k) of each elastic band used in the Manubot. The experimental setup involved suspending the elastic bands from a fixed support at one end and then applying known weights to the other end to measure the spring coefficient. An analytical balance (ME204TE, Mettler Toledo) was used to determine the object's mass. The change in elongation (ΔL) of the elastic bands was measured using digital calipers. Three ring-shaped elastic bands were tested, with diameters of 9.5 mm, 7.9 mm, and 25.4 mm, respectively. Using Hooke's Law ($k = F/\Delta L$), the spring coefficients were calculated as k = 59.6, 80.8, and 134.2 N m^{-1}, corresponding to the most flexible, intermediate flexible, and less flexible rubber bands, respectively.

2.4. Imaging and image processing

A high-speed camera (Photron FASTCAM MINI AX, frame rate = 2.000 fps) mounted with a Nikon Zoom lens (70–200 mm f/2.8G ED VR II AF-S, Nikkor) was used to capture the impact of solid bodies on water, along with the resulting cavity formation and Worthington jet dynamics. The water tank was illuminated from two angles, with a light diffuser attached to the water tank.

The kinematics and angular opening dynamics of the projectile were measured by tracking its apex, while for the Manubot, three points were tracked, two at the edges and one at the apex (or centre) of the solid bodies. We used the Photron Fastcam Analysis (PFA), Photron Fastcam Viewer (PFV4), and DLTdv8 (a MATLAB-based digitizing tool) to track the coordinates of these points frame-by-frame. To quantify the Worthington jet, we measured the splash height in PFV4 and the jet area using a custom MATLAB script. As a metric for the splash size from the Manubot, we quantified the splash area as the Worthington jet region above $y > 0.1 L_m$, where L_m is the Manubot's single arm length. The raw image of the water splash is binarized with a threshold of 0.5, where 0 and 1 denote the black and white colour, respectively. Small areas less than 50 pixels are detected as the droplet and removed, so only the splash region is visualized. Finally, the inner area of the jet was filled with a region identification algorithm and measured across all time steps.

3. Results and discussion

3.1. Manu jumping in humans

3.1.1. Aerial manoeuvres and the V-shape entry

A Manu jump comprises four distinct stages: water entry in a V-formation, a rollback and kick motion underwater to enlarge the air cavity, the closure and collapse of the air cavity, and the formation of a Worthington splash. Figure 1a shows an overlay of sequential snapshots illustrating the step-by-step aerial manoeuvres of an individual performing a Manu jump from a diving board into a swimming pool. To gain momentum, the individual pushes the diving board downward (steps 1–2) before jumping vertically into the water executing an 'utkatasana' pose (steps 3–4). During vertical free fall, the individual folds their body into an L-shape (step 5) before water entry while transitioning to a V-shape upon water entry (step 6).

A more holistic depiction of a Manu jump covering both aerial and underwater manoeuvres to create a large Worthington splash is presented in figure 1b. In addition to executing the aerial transitions into a V-shape at water entry, Manu jumpers perform underwater manoeuvres. These include a rollback and kick motion, where they extend their bodies underwater, moving their head and back downwards while their feet point upwards. This movement expands the air cavity, which eventually reaches its maximum size before collapsing and closing at a pinch-off point, forcing water upwards in the form of a Worthington splash. Figure 1c shows a sequence of snapshots of an individual performing an underwater body expansion. Before entering the water, Manu jumpers bend their body while keeping their back straight, forming a V-shape. This water entry creates a crown splash (figure 2d, inset of the second snapshot), deforming the water surface and initiating the formation of an air cavity. If the body remains compact, the cavity will likely close and collapse. However, Manu jumpers counteract this by extending their body underwater, rolling backward and kicking downward to enlarge the air cavity (third snapshot). Eventually, the cavity collapses and pinches off (fourth snapshot), forcing the liquid rapidly upward to create a splash, as shown in the final snapshot inset of figure 2d.

From human jumping video observations, we hypothesize that the underwater manoeuvres performed by Manu jumpers not only enlarge the air cavity but also delay its pinch-off, enabling stronger gravitational forces to retract the deformed water surface and generate a larger Worthington splash. These underwater movements are thus crucial in popping a big Manu splash, particularly when other factors like jumping height and body dimensions are similar.

Manu jumping, as a recreational sport, invites creativity and personal flair, with individuals showcasing aerial manoeuvres like backflips and diving from various platforms such as docks, cliffs, trees, diving boards, and pool edges. Figure 1d illustrates the body orientation of Manu jumpers during various types of Manu jumps, based on frames extracted from YouTube videos. In the first sequence, a jumper performs a Manu jump from a shallow height (poolside), forming the V-shape quickly due to the limited fall distance. In the second sequence, corresponding to the jump shown in figure 1a, the individual leaps from a diving board, descends vertically, and folds their legs to form a V-shape before water entry. In the third instance, the jumper uses a diving board to generate upward momentum for a backflip, skilfully controlling their orientation to achieve a V-shape upon water entry (figure 1d). Despite differences in height and aerial manoeuvres, all jumps consistently result in a V-shape at water entry. The median V-angle during water entry of human Manu jumpers was approximately 46.36° (figure 1e).
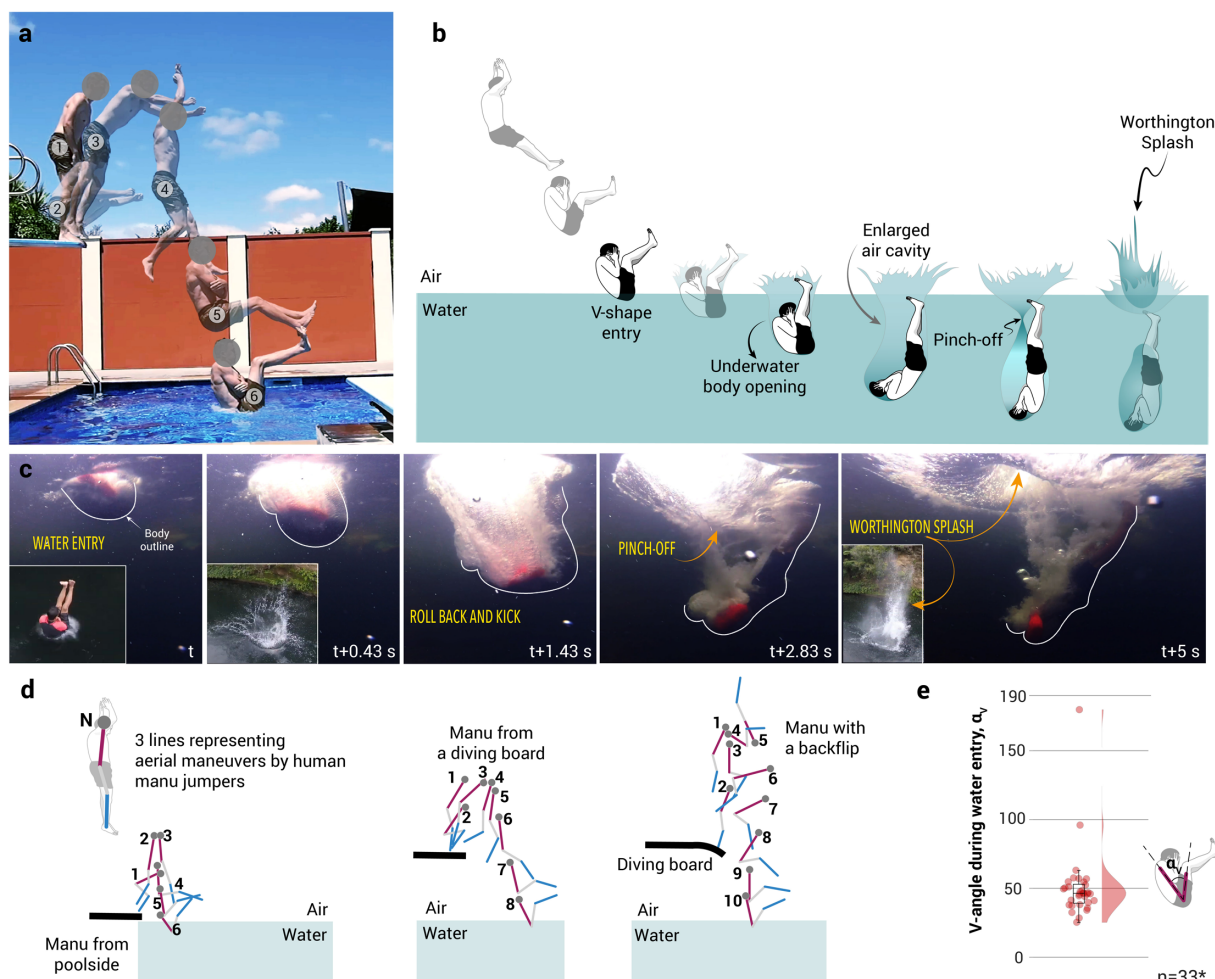
Figure 1. (a) A composite image showing a human performing a Manu jump, illustrating the successive stages of aerial manoeuvres, leading to a V-shaped entry into the water (video credits: Bradford | Youtube). (b) Illustration describing a human performing a Manu jump. (c) Water entry and subsequent opening of human underwater to enhance the size of the air cavity to create a Worthington splash (video credits: Bomb School | Youtube). (d) Different types of aerial manoeuvres to form a V-shape at water entry. (e) V-angle formed by humans entering the water to pop a Manu splash. Median V-angle, $\alpha_v = 46.36$ with a standard deviation of approximately 26.29 ($n = 33$).
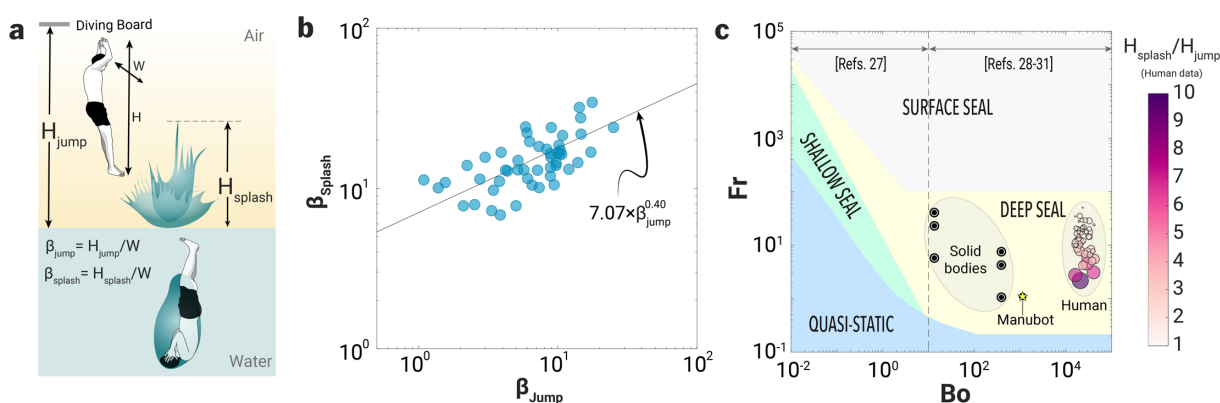

Figure 2. Effect of jumping height and underwater dynamics on the splash height in Manu jumping. (a) Jumping and splash parameters illustrated for a Manu jump. (b) Dimensionless splash height (β_{splash}) versus dimensionless jumping height (β_{jump}), $n = 50$. The solid line represents a power law fit to the Manu jumping data (coefficient of determination, $R^2 \approx 0.41$). (c) Regime map for the cavity shape created by the water entry of solid spheres, solid shapes [31–35], humans performing Manu jumps and the Manubot.

3.1.2. Human kinematics in Manu jumping

Apart from entering the water in a V-formation, underwater manoeuvres play a key role in generating a Manu splash. When humans enter the water, their impact deforms the surface, creating a large air cavity. In this process, the inertial forces of the body temporarily overcome the gravitational forces that maintain the water surface to be flat ($Fr > 1$). As the gravitational pull of the water overcomes the inertia of the human body, the air cavity collapses and pinches off. This collapse rapidly displaces water upward from the pinch-off point, driving the formation of an accelerating jet or a splash that ascends until surface tension and
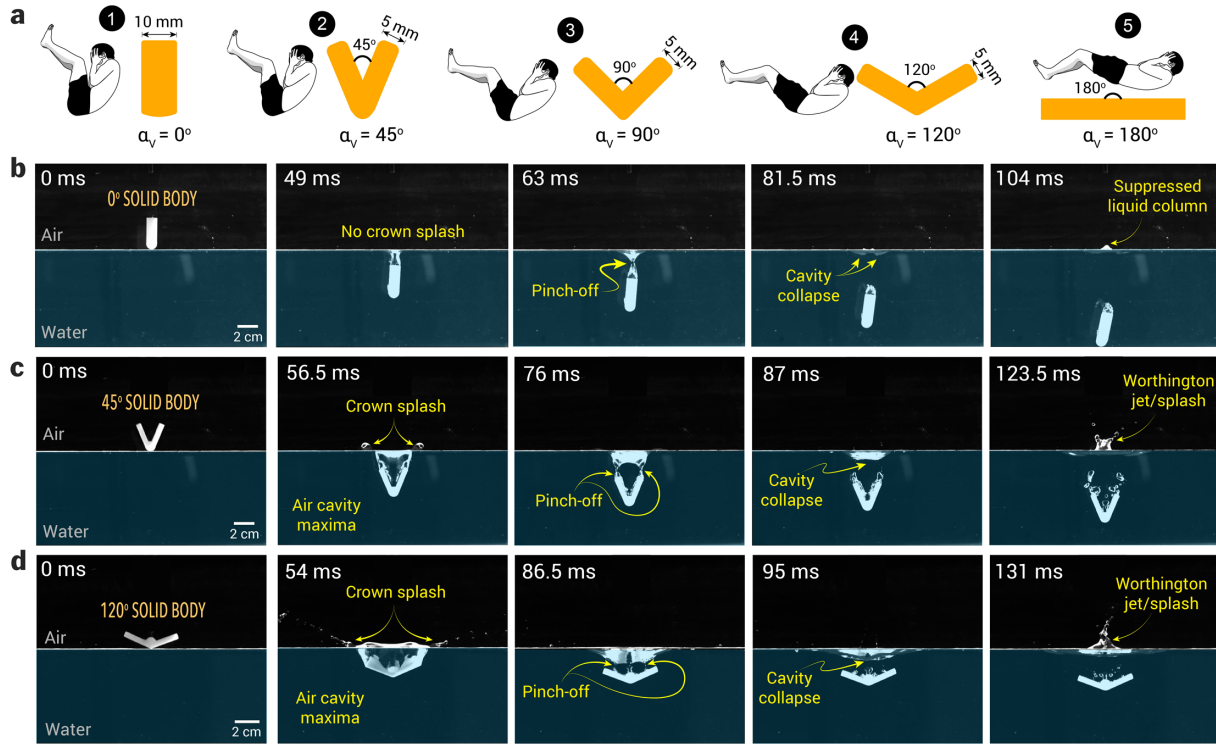
Figure 3. Water entry dynamics of solid bodies with varying V-angles (α_v). (a) Solid bodies and their corresponding human formation during water entry in our study. Human bodies are $\approx \mathcal{O}(10^2)$ times larger than solid bodies. Sequence snapshots of (b) a straight solid body ($\alpha_v = 0°$) entering water at an impact speed of 0.75 m s^{-1} which generates a small air cavity and a shallow pinch-off point, forming a suppressed liquid column, (c) a solid body with $\alpha_v = 45°$ entering the water at a speed of 2 m s^{-1}, generates a larger air cavity that pinches off at two points, resulting in a bifurcated Worthington splash and (d) a solid body with $\alpha_v = 120°$, entering the water at a speed of 1.5 m s^{-1}, generating a wider air cavity forming a single pinch-off point, resulting in a focused Worthington jet.

gravity dominate, decelerating its ascent. Eventually, the jet or splash halts and falls back into the water. For human data, we studied the effect of varying the take-off height (H_{jump}) on the splash height (H_{splash}).

Increasing the height of the jump increases the impact speed (u) of the Manu jumper on the water surface, i.e. $u \propto \sqrt{H_{jump}}$. In Manu jumping championships, the maximum jumping height is limited to 10 m to ensure the safety of the participants. While jumping height is a critical factor, participants' body size and underwater manoeuvres also significantly influence the resulting splash height. However, since the YouTube data used in our analysis lack information on body weight, our study focuses on the effect of jumping height on splash dynamics. We examined the effect of dimensionless jumping height ($\beta_{jump} = H_{jump}/W$, where W is the width of the Manu jumper) on the dimensionless height ($\beta_{splash} = H_{splash}/W$) of the resulting Worthington jets (see definition of these dimensions in figure 2a). The dimensionless splash height increased with jumping height as $\beta_{splash} \sim 7.07\beta_{jump}^{0.40}$ (figure 2b). The cavity pinch-off dynamics in human Manu jumps can also be characterized using Froude number (Fr) and Bond number (Bo) plots [32]. For similar Bo, H_{splash}/H_{jump} ratios decreased with increasing Fr. This suggests that for increasing $Fr(\propto u)$, H_{splash} does not increase linearly with increasing H_{jump}. Human water entry during Manu jumps falls within the deep seal regime, specifically in the range of $10^4 < Bo < 10^5$ and $1 < Fr < 100$ (figure 2c). This indicates that the inertial forces of the human body entering the water during a Manu jump dominate the surface tension and gravitational forces. Similarly, the other shapes used in this study also fall within the deep seal regime, highlighting consistent dynamics across different configurations of passive and active projectiles.

3.2. Splash dynamics of solid projectiles

3.2.1. Water entry, cavity formation and the Worthington splash

We visualized the water entry of V-shaped projectiles (or wedges) at varying impact speeds to qualitatively compare their entry dynamics, focusing on the formation of air cavities that close and collapse to produce Worthington splashes. We studied the water entry dynamics of projectile shapes with V-angles of 45°, 90°, and 120° (figure 3a)—investigating cavity formation and Worthington splash characteristics to elucidate the role of the V-angle in human Manu jumping. Additionally, we used a flat vertical shape ($\alpha_v = 0°$) simulating a human folding their body to align their back and legs parallel to upward, and a flat horizontal projectile representing the scenario of a human landing on water flat on their backside ($\alpha_v = 180°$).

Here, we present sequential snapshots of water entry and Worthington jet formation for three representative cases with $\alpha_v = 0°$, 45°, and 120°, representing the most commonly observed conditions in human water entry. These projectiles generated a range of Worthington splashes, from the smallest to the largest, resulting from cavity collapse after their water entry at varying impact speeds.

Case (i): A solid projectile with $\alpha_v = 0°$ impacts the water at a speed of 0.75 m s^{-1}. Due to its elongated shape, the width of the air cavity formed closely matches the width of the projectile itself and collapses almost immediately after the body is fully submerged ($t = 49$ ms), resulting in minimal to no crown splash. After the air cavity pinches off, it collapses ($t = 81.5$ ms), displacing water upward to form a suppressed liquid column, with its maximum height captured in the final snapshot ($t = 104$ ms). In competitive diving, athletes often adopt this shape upon entry and quickly transition to an L-shape underwater to ensure the cavity collapses as close to the surface as possible, minimizing or eliminating splashes.

Case (ii): In another representative sequence of snapshots showing the water entry of solid projectiles, a body with a $\alpha_v = 45°$ impacts the water at a speed of 2 m s^{-1}, creating a crown splash ($t = 56.5$ ms) and trapping a large volume of air compared with the first case. Notably, as the body descends further into the water, the air cavity closes, forming two distinct pinch-off points ($t = 76$ ms) at the trailing edges of the projectile. As the air cavity pinches off, two jets emerge from the pinch-off location in an upwards direction ($t = 87$ ms), which merge to form a forked Worthington splash ($t = 123.5$ ms). This case represents the majority of the water-entry cases of the Manu jumpers, where the median angle of water entry is approximately 48°. It is important to note that in human Manu jumping, the human body and the resulting air cavity formed in the water are not symmetric, unlike the projectiles studied. This asymmetry leads to the formation of irregular and asymmetric Worthington splashes (last snapshot in figure 1c).

Case (iii): The third representative case of Manu jumping involves the water entry of the solid projectile with a 120° V-angled solid projectile impacting water at $u = 1.5$ m s^{-1} (figure 3d). The water entry of this shape created a larger air cavity ($t = 54$ ms) in the water, accompanied by a wide crown splash in comparison with the prior cases. The proximity of the trailing edges of the V-shaped projectile and the bolt attached at its apex to secure it to the electromagnet interferes with the air cavity's pinch-off dynamics. This interference results in three pinch-off points ($t = 86.5$ ms) merging into a single upward-moving fluid curvature ($t = 95$ ms). This cavity eventually collapses, producing a single jet-like splash ($t = 131$ ms). Additionally, the 120° configuration generates two flat water curtains on either side of the shape, merging to form a single splash (electronic supplementary material, video S1).

The impact speed (u) and the V-angle of the solid projectile shapes affect the air cavity pinch-off depth (H_{po}) and the projected area of the cavity at the pinch-off ($A_{c,po}$); these parameters collectively affect the Worthington splash outcomes, quantified in terms of the maximum splash height (H_{max}) and the maximum Worthington splash area ($A_{s,max}$). Various stages of a solid projectile entering the water, creating an air cavity and a crown splash, and finally a Worthington splash following the air cavity pinch-off are illustrated in figure 4a. The average pinch-off depth of air cavities increased with decreasing α_v from 120° to 45° (figure 4b), whereas the pinch-off depth was similar for 180° and 120° shapes. For the 0° solid projectile entering water at $u = 1.5 - 2$ m s^{-1}, air cavity dynamics differ due to a thinner cavity formed by a single edge in its wake, leading to lower pinch-off depths compared with the 45° projectile, which generates wider cavities with two edges and results in larger pinch-off depths at similar impact speeds. With increasing impact speed, the drag force on the projectiles increases ($F_D \propto u^2$) and therefore, the pinch-off depths were shallow for high-impact speed water entry of 0° solid projectiles (figures 4b, 10). For other shapes, the geometry of the solid projectiles influences the drag force, resulting in a nonlinear relationship between pinch-off depth and impact speed (figure 4b).

3.2.2. Projectiles with $\alpha_v = 45°$ generate fastest Worthington jets

The 45° solid projectile entering water at $u = 2$ m s^{-1} ($H_{po} \sim 30$ mm) produced the fastest Worthington splash, with maximum speed reaching up to $v_j \sim 2$ m s^{-1} (figure 4c). Meanwhile, other angled shapes (90° and 120° for all impact speeds) and 45° shape (0.75 and 1.5 m s^{-1}) exhibited jet speeds between 0.2 and 1 m s^{-1} for pinch-off depths ranging from 12 to 30 mm. For the vertical shape ($\alpha_v = 0°$), water entry produced suppressed liquid columns at lower impact speeds ($u = 0.75$ m s^{-1}) and focused tall jets at higher impact speeds ($u = 2$ m s^{-1}). The maximum jet speeds for this shape, regardless of whether the pinch-off point was shallow or deep, fell within a range of $v_j \sim 0.3 - 0.4$ m s^{-1}. The flat shape ($\alpha_v = 180°$) generated Worthington splashes with relatively slower jet speeds, ranging between 0.1 and 0.3 m s^{-1} across varying impact speeds.

3.2.3. The role of the pinch-off depth and the cavity size in the Worthington splash

We studied the effect of varying V-angles of solid projectiles on pinch-off depth (H_{po}) and air cavity size ($A_{c,po}$), and their subsequent effects on splash height (H_{max}) and splash area ($A_{s,max}$) (figure 4d,e). The solid projectile with $\alpha_v = 0°$ entering water at $u = 0.75$ m s^{-1} produced the shortest Worthington jet, or a suppressed liquid column ($H_{max} \sim 2.2$ mm), with a pinch-off depth (H_{po}) of 16 mm and the smallest cavity area (500–700 mm^2). At a higher impact speed of 2 m s^{-1}, the same projectile shape produced the tallest Worthington jet ($H_{max} \sim 200$ mm), forming a cavity with an area of approximately 16 000 mm^2 and pinching off at a depth of $H_{po} \sim 55$ mm. Due to the thinner Worthington jets produced by this shape, their maximum projected area remained the smallest, approximately 500–600 mm^2, across varying impact speeds (figure 4f and to row of 5). When this shape was dropped parallel to the water surface ($\alpha_v = 180°$) at a low impact speed of 0.75 m s^{-1}, the splash height ranged from 15 to 25 mm, with an air cavity area of around 1500 mm^2 at a pinch-off depth (H_{po}) of 12–14 mm. At a higher impact speed of 2 m s^{-1}, the splash height increased significantly to approximately 60 mm (with splash projected area of 1200–1300 mm^2), with a pinch-off depth of 50–60 mm and an air cavity size ($A_{c,po}$) of 2500–3000 mm^2.

For solid projectiles with α_v ranging from 45° to 120°, the splash height (H_{max}) increased with impact speed during water entry (figure 4d,e). However, the variation in splash area was not significant, indicating that larger V-angles result in wider but shallower splashes. Among the angled shapes, the 45° projectile produced the tallest splash (approx. 100 mm with $A_{s,max}$ of approx. 1200 mm^2) corresponding to a pinch-off depth of approximately 32 mm and a cavity area of approximately 1200 mm^2. At an impact speed of 1.5 m s^{-1}, the splash heights were comparable across different angled projectiles; however, the 45° shape exhibited the deepest pinch-off depth and a smaller cavity area than wider angle shapes (figure 5d,e). In Manu jumping, the air cavity created
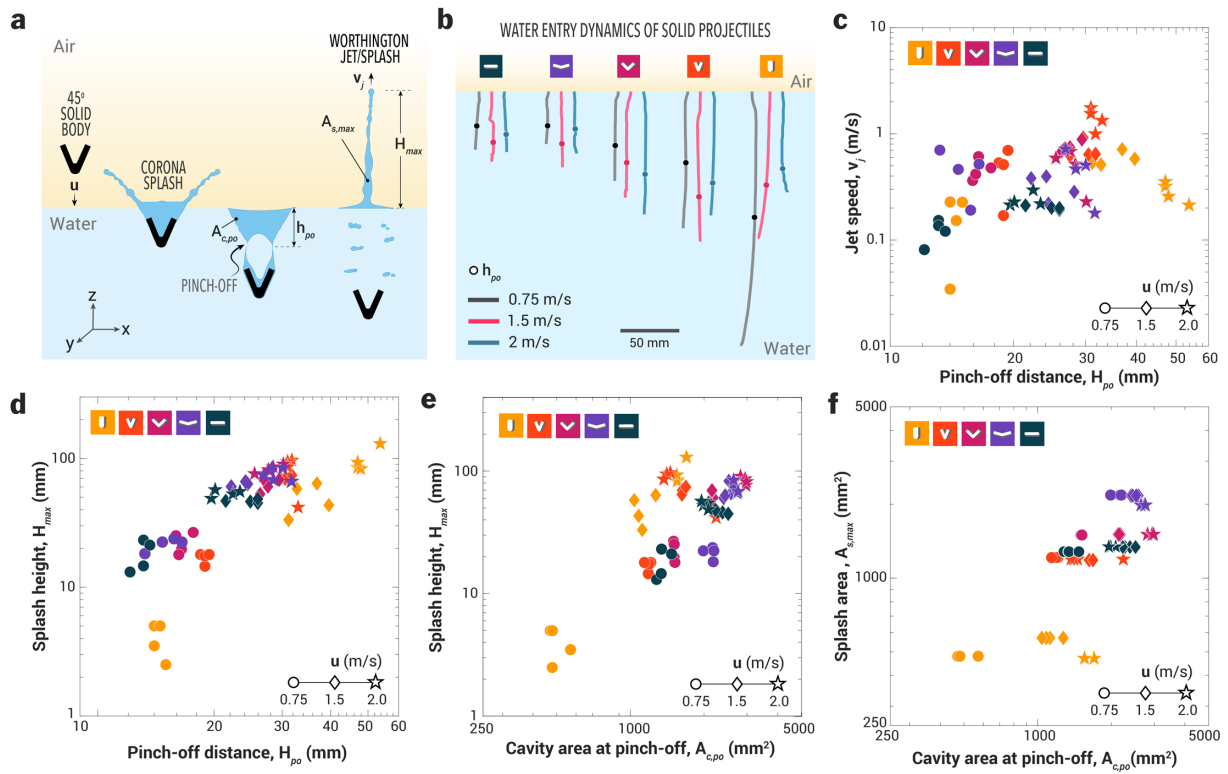
Figure 4. Splash dynamics of solid projectiles entering water at different impact speeds (0.75–2 m s^{-1}). (a) Schematic showing a 45°-shaped projectile entering water at an impact speed of u m s^{-1}. The impact creates a corona splash as the projectile deforms the water surface, forming an air cavity that pinches off and collapses, generating a Worthington jet with a height of H_{max} and a maximum splash area of $A_{s,max}$. (b) Trajectories and pinch-off depths of air cavities formed by various solid projectiles entering the water at different impact speeds. (c) Relationship between pinch-off depth and Worthington jet speed, (d) splash height as a function of pinch-off depth, and (e) effect of varying pinch-off depth to enlarge the cavity area at the pinch-off point, and (f) Worthington splash area as a function of cavity area at the pinch-off point. Note: each data point represents a single trial, with four replicates conducted for each experimental condition.

by the human body dictates Worthington jet dynamics. The 45° shape demonstrates that a smaller cavity area but deeper air cavity pinch-off can generate splash heights comparable with those of wider angles (90° and 120°), potentially reducing the risk of injury.

The snapshots of the maximum splash height for various shapes entering the water at varying impact speeds are shown in figure 5. At low impact speeds ($u = 0.75$ m s^{-1}), the splash size and shape increased with increasing V-angle, where 0° shape forms a minimal splash, the 45° shape forms a forked jet, and the 120° creates a small and thick jet. At medium impact speeds of $u = 1.5$ m s^{-1}, the solid body with a 0 degree angle creates a bigger splash than its lower speed counterpart, while the Worthington jets from shapes like 45° and 120° cover a greater splash area. Notably, the 45° shape, achieves a higher splash height than other shapes at an impact speed of 1.5 m s^{-1}. Further, an increase in impact speed to 2 m s^{-1} for the 0° shape resulted in the tallest jets with focused tips, tall jets with a wider base for the 45° shape and a shallow jet with satellite drops for the 120° shape at this highest impact speed.

Although V-angled projectiles offer insights into the effect of V-angle and impact speed on Worthington splashes, they lack the active underwater movements of human Manu jumpers. To address this, we developed a robotic system capable of executing controlled underwater manoeuvres, enabling the creation of large, asymmetric Manu splashes that closely resemble the Manu splashes generated by humans.

3.3. Manubot

3.3.1. Timely body opening increases Worthington jet strength

Using high-speed imaging, we elucidate the role of the onset of the body opening of Manubot (figures 6a and 9) on the Worthington jet dynamics. Here, the time (t) is normalized with the impact velocity (u) of Manubot and its arm length (L_m), defining dimensionless time as $\hat{t} = tu/L_m$. The dimensionless body opening time is defined as $\hat{t}_r = t_r u/L_m$, where t_r represents the body opening time, which can be controlled by the signal from the microprocessor. Before studying the effect of underwater opening, we investigate the role of the tilt angle of the Manubot (θ_{tilt}, the angle between the gravity direction and the centreline of the robot) in the splash size. To enhance the splash generation, we determined the tilt angle for Manubot water entry ($\alpha_v = 45°$) to be 30° (figure 6c–e and electronic supplementary material, video S2). At a small tilt angle (figure 6c), the impact creates two separate air cavities ($\hat{t} = 2.9$), followed by a weakly developed Worthington jet ($\hat{t} = 3.5$). For a high tilt angle case (figure 6d,e), a single air cavity forms on the right side of the Manubot, concentrating and strengthening the Worthington jet. However, at excessively high tilt angles (figure 6e), the left side of the robot obstructs jet development ($\hat{t} = 3.5$). Thus, a tilt angle of $\theta_{tilt} = 30°$ for solid projectiles enhances the size of the Worthington splash (figure 6d). To fully understand the effect of tilt angle in humans jumping into the
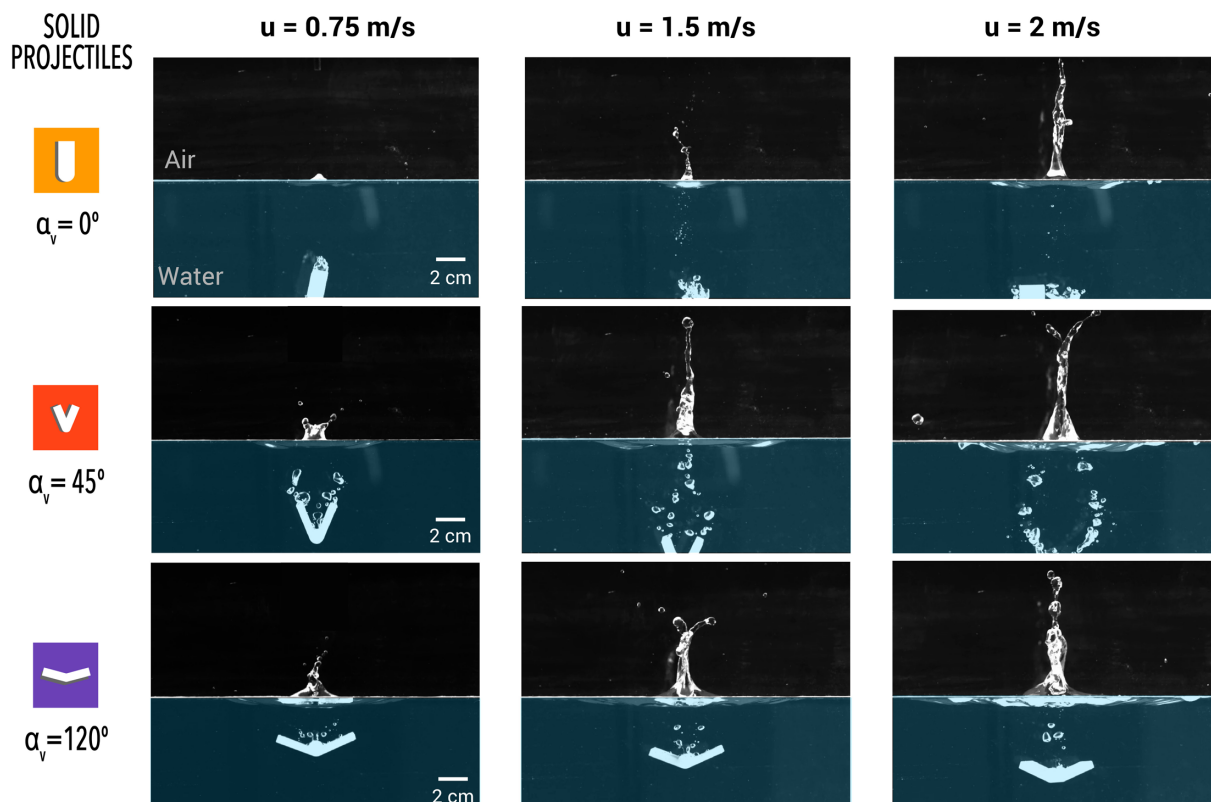
Figure 5. Snapshots showing the maximum height of Worthington jets achieved for water entry of solid objects with varying V-angles and impact speeds.

water and the associated injury risks, further investigation is needed, including high-speed imaging of human dives and impact force measurements.

After falling from the initial height ($h \simeq L_m$ where L_m is the arm length of Manubot), the Manubot makes contact with water at $\hat{t}_r = 1.0$, and depending on the body opening time ($\hat{t}_r$), different cavity and splash dynamics occur as follows (figure 6f–h and electronic supplementary material, video S2):

Early opening ($\hat{t}_r < 1.1$): The early opening case (figure 6f) corresponds to when the Manubot unfolds its body before water contact or at a shallow depth ($< 0.5L_m$). The right side of the robot pushes water downward, creating a large drag, while the left side remains mostly exposed to air ($\hat{t} = 1.7$). This configuration creates counterclockwise torque as two robot parts expand, and the robot eventually orients itself parallel to the water surface. Here, the accelerated left part of the robot arm creates a large splash at $\hat{t} = 2.7$. The increased contact area increases the drag force, significantly decelerating the robot's submergence. During the impact, two air cavities are formed on both the right and left sides (with the right cavity volume larger than the left) and pinch off at a shallow depth of $\hat{H}_{po} = H_{po}/L_m = 0.34$. The weak Worthington jets are generated on both sides due to the dissipation of the Manubot's potential energy into two Worthington jets.

Timely opening ($1.1 < \hat{t}_r < 1.5$): At this time range, the body opens when the robot is submerged at $\sim 0.5L_m$ at $\hat{t} = 2.0$. Since the left side is sufficiently submerged, the right side of the robot can resist the counterclockwise torque and further push fluid downward, deepening the pinch-off depth to approximately $0.7L_m$. Therefore, the formation of the air cavity and the Worthington jet is concentrated on the right side, creating a large water column on the right side of the robot.

Late opening ($1.5 < \hat{t}_r < 2.8$): In the late opening case (figure 6h), the body expansion starts nearly at the pinch-off time ($\hat{t} \sim 3$). Since the air cavity has already been developed, the opening movement does not significantly affect cavity collapse or the strength of the Worthington jet. However, the jet shape is affected by the body opening time (figure 7a), which will be discussed later.

No-opening ($\hat{t}_r > 2.8$): When the body opening occurs sufficiently late, its movement becomes completely irrelevant to the cavity dynamics, including cavity formation and Worthington jet generation, and can be regarded as an effectively no-opening case.

3.3.2. Timely opening deepens the pinch-off and enables the vertical Worthington jet

The area of the Worthington jet has been quantified by the binarization of light intensity of high-speed images with a threshold of 0.5 [36]. Figure 7a confirms that the maximum area and height of the Worthington jet occur in the timely opening regime, while a mismatch in timing results in jet deflection in the early and late opening cases. The no-opening case produced a weaker water jet (figure 7a). For all times, the area of the Worthington jet (normalized by the square of one side length of the robot, L_m^2) in the timely opening case, outperforms the other cases, which are comparable with each other (figure 7b). Figure 7c shows that this maximum Worthington jet area can only be achieved when the robot starts to release within a narrow range of time ($1.1 < \hat{t}_r < 1.5$), implying that accomplishing a perfect Manubot performance for humans requires subtle body manoeuvring. The jet area decreases monotonically as time increases from $\hat{t}_r = 1.5$, reaching its local minimum at $\hat{t}_r = 2.5$. For $2.8 < \hat{t}_r$, the jet area saturates to approximately 0.4 at which the body movement no longer affects the jet formation.
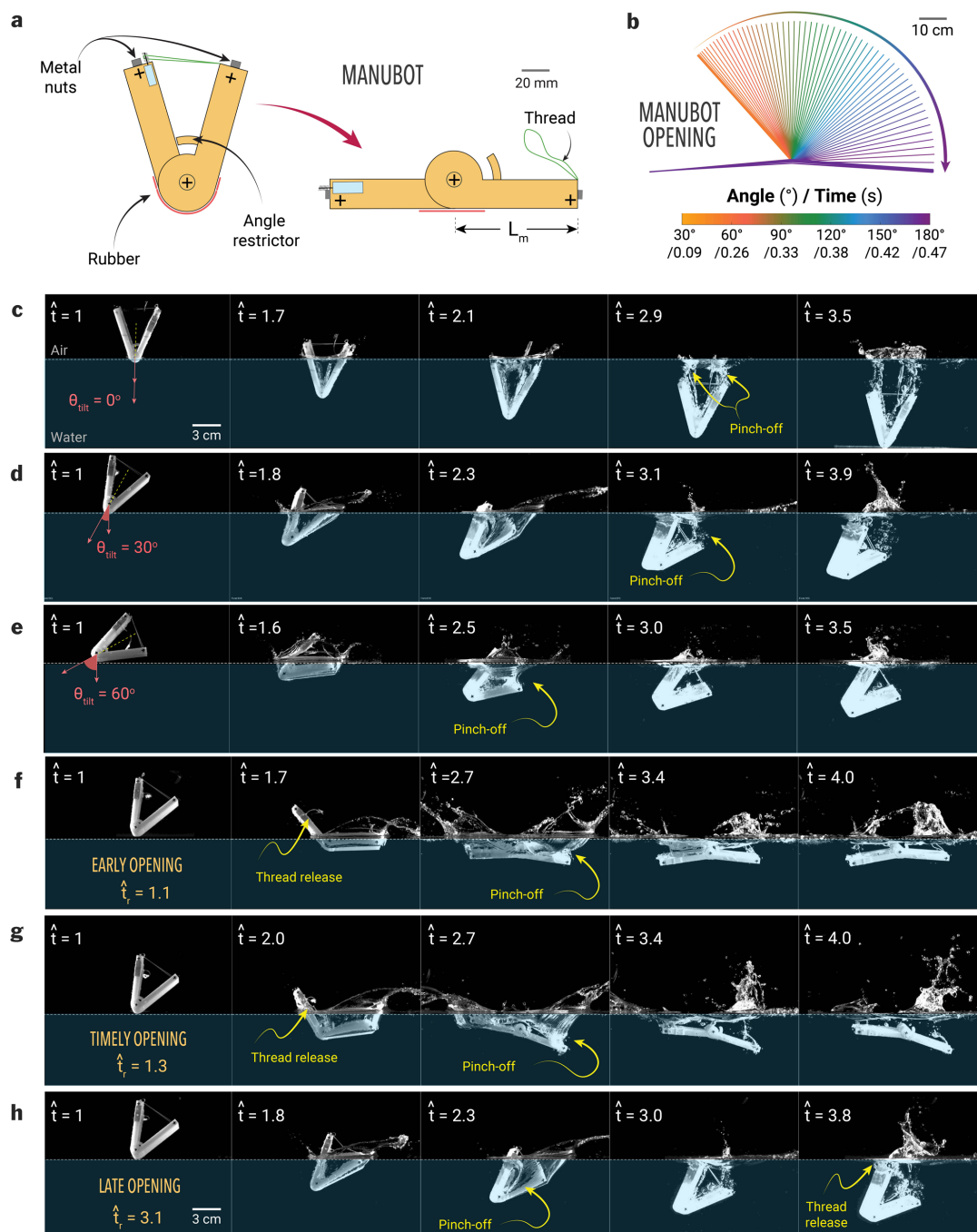
Figure 6. Manubot and its water entry with varying body tilt angles (θ_{tilt}) and body opening times ($\hat{t}_r$). (a) Manubot with release mechanism and expanding rubber. (b) Speed of Manubot's motion. (c–e) Water entry of Manubot without body opening ($\hat{t}_r \rightarrow \infty$) with various tilt angle of (c) $\theta_{tilt} = 0°$, (d) $\theta_{tilt} = 30°$ and (e) $\theta_{tilt} = 60°$. (f–h) Time sequence of Manubot falling on the water surface depending on the release time: (f) early opening ($\hat{t}_r = 1.1$), (g) timely opening ($\hat{t}_r = 1.3$) and (h) late opening ($\hat{t}_r = 3.1$). Here, the Manubot is shown from the moment it comes into contact with water at $\hat{t} = 1$, which starts to fall at $\hat{t} = 0$. Note that the thread in (a) was used to maintain the V-angle of the Manubot, and it did not open up in cases shown in (c–e).

The opening time ($\hat{t}_r$) for four regimes has been identified in figure 7d: early opening ($\hat{t}_r < 1.1$), timely opening ($1.1 < \hat{t}_r < 1.5$), late opening ($1.5 < \hat{t}_r < 2.8$) and no-opening ($2.8 < \hat{t}_r$). In terms of pinch-off time ($\hat{t}_p$, defined as $\hat{t}_p = t_p \boldsymbol{u}/L$ where t_p is pinch-off time), the air cavity pinches off at $\hat{t}_p = 2.8$ without body opening, i.e. the no-opening case, and the pinch-off is slightly delayed for all opening cases: $\hat{t}_p = 3.2$ (early opening), $\hat{t}_p = 3.6$ (timely opening) and $\hat{t}_p = 2.9$ (late opening). This delay is attributed to the increased impact velocity, which creates a wider air cavity and, thereby, delays the pinch-off incident.

The timely opening case delays pinch-off the most (figure 7d) and also achieves the greatest depth (figure 7e), as the right side of the robot can effectively push water downward, contributing to cavity formation. For the timely opening case, the depth and time of pinch-off increase by approximately 30% and 15%, respectively, compared with the no-opening case.

The jet angle follows an interesting trend (figure 7f): as $\hat{t}_r$ increases from 0.8 to 2, the jet angles gradually increase from 60° to 120°, achieving vertical (90°) at the timely opening at $\hat{t}_r = 1.3$. At $\hat{t}_r = 2$, the jet direction suddenly transitions to 50° and saturates at 70° from $\hat{t}_r = 2.8$. The vertical (90°) Worthington jet can be achieved either within a narrow range of timely openings ($1.1 < \hat{t}_r < 1.5$) or in cases with no opening ($\hat{t}_r > 2.8$).
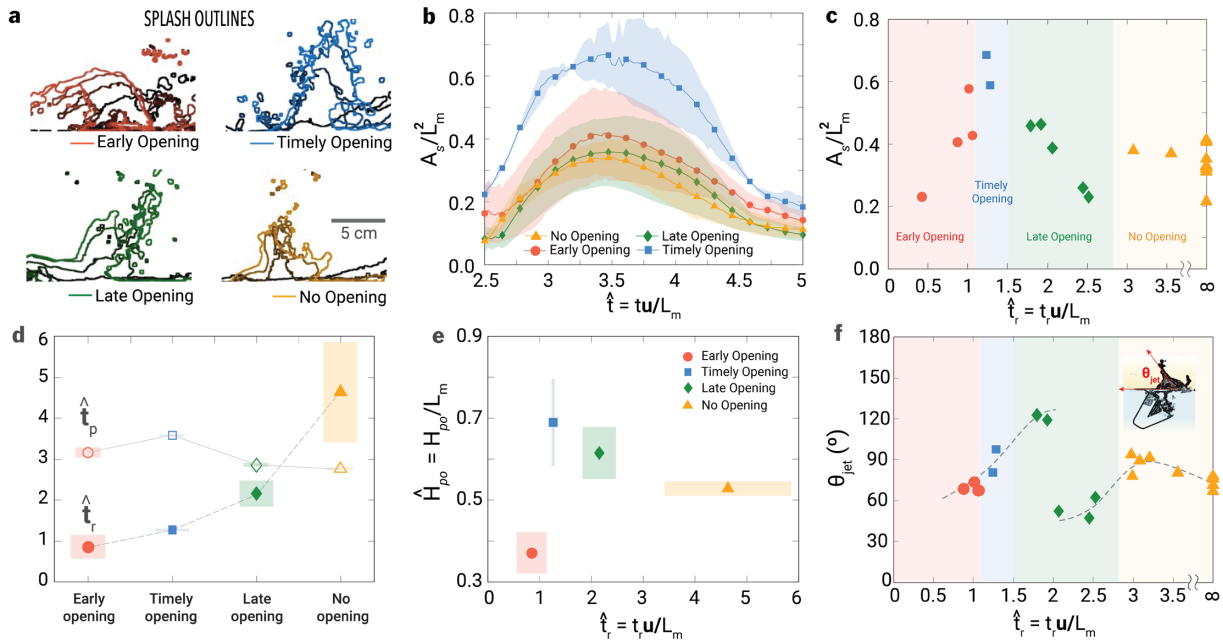
Figure 7. Splash and cavity dynamics of Manubot with varying body opening time ($\hat{t}_r$). (a) Overlay of splash development with time interval of $\hat{t} = 0.3$, (b) time-dependent splash area (A_s) normalized with robot arm length (L_m^2), (c) dimensionless splash area (A_s/L_m^2) at $\hat{t} = 3.5$, (d) averaged body opening time ($\hat{t}_r$, open symbols) and averaged pinch-off time ($\hat{t}_p$, closed symbols) depending on cases, (e) the normalized cavity depth ($\hat{H}_{po} = H_{po}/L_m$, where H_{po} is the cavity depth) at pinch-off and (f) the jet direction (θ_{jet}). Here, a total of 20 trials were conducted with the Manubot across all regimes: four for early opening, two for timely opening, and five for late opening and nine for no-opening. The shading in (b,d,f) indicates the error bar. $\hat{t}_r$ in (d) for the no-opening case exhibits a large error bar due to the absence of an upper limit.

3.3.3. Timely energy transfer enhances the Worthington splash size

The Manubot releases each potential energy differently to its environment depending on the body opening timing (figure 8a). The submergence depth increases as the body opening is delayed (figure 8b) because the folded body experiences lower drag than other opening cases, allowing it to fall faster (figure 8c). Depending on the body opening time, the slope of the body angle also differs after release (figure 8d): timely ($\hat{t}_r > 1.3$) and late opening cases ($\hat{t}_r > 1.9$) have more gradual curves than the early opening case ($\hat{t}_r > 0.9$). This implies that robot expansion decelerates due to drag, and momentum transfer between the robot and water is active for the timely and late opening cases.

From the perspective of energy conservation, the Worthington jet is energized by two potential energies: the gravitational energy of Manubot ($E_p = mgh$, where m, g, and h are the mass of Manubot, gravitational acceleration, and vertical position of Manubot, respectively) and the elastic energy stored in the initially extended rubber in the robot ($E_e = \frac{1}{2}\Sigma k\Delta x^2$, where Σk is the sum of the spring coefficients of the rubber used in Manubot, and Δx is the displacement of the rubber proportional to the V-angle).

These two potential energies are transferred to the translational and rotational kinetic energy of Manubot ($E_k = \frac{1}{2}mv^2$, where v is the vertical velocity of Manubot, and $E_{rot} = \frac{1}{2}I\omega^2$, where I and ω are the moment of inertia and angular velocity of Manubot) and subsequently to the mechanical energy of water ($E_{m,w}$, the sum of kinetic and gravitational potential energy of water). Some of this energy ($E_{m,w}$) is temporarily stored as the gravitational potential energy of the Worthington jet (E_w) at its highest position, eventually vanishing through the viscous dissipation.

To understand how energy flows, the energy distribution has been calculated in figure 8e. The gravitational potential energy of the Worthington jet (E_w) is estimated from the jet area in figure 7a by assuming it forms a circular cone with a cone angle of 45° with the same cross-sectional area. Here, the rotational kinetic energy of Manubot is neglected due to the small change in tilted angle (see figure 8a), and the air kinetic energy is neglected due to the low air density. Capillary energy and viscous dissipation significantly influence droplet generation and other small-scale phenomena like bubble bursting [17]. These factors are omitted here because this study focuses on large-scale features such as the cavity and Worthington jet. All energy is normalized with the initial gravitational potential energy of Manubot ($E_{p,0}$), measured at $\hat{t} = 0$. Figure 8e shows that the gravitational potential energy (E_p) decreases from $\hat{t} = 0$ to 2 while the kinetic energy (E_k) increases from zero and subsequently decreases after water contact ($\hat{t} \simeq 1$), attributed to the hydrodynamic drag. For the opening cases, the elastic potential energy (E_e) begins to decrease, releasing energy at $\hat{t}_r = 0.9$, 1.3, and 1.8 for early, timely, and late opening, respectively. Despite this temporal difference of E_e, the potential energy of the Worthington jet (E_w) for all cases emerges from $\hat{t} = 2.5$ and peaks at $\hat{t} = 3.5$, because the pinch-off time ($\hat{t}_p$) remains consistent regardless of body opening time ($\hat{t}_r$), as described in figure 7d. However, the maximum jet potential energy ($E_{w,max}$) is significantly influenced by $\hat{t}_r$: $E_{w,max}/E_{p,0} = 0.22$ (for $\hat{t}_r = 0.9$, early opening case), 0.55 ($\hat{t}_r = 1.3$, timely opening case), 0.16 ($\hat{t}_r = 1.8$, late opening case) and 0.14 ($\hat{t}_r \to \infty$, no-opening case) (figure 8e).

Figure 8f–i shows three energy fluxes for the mechanical energy of Manubot ($\dot{E}_p + \dot{E}_k$), the elastic potential energy of Manubot ($\dot{E}_e$), and the gravitational potential energy of the Worthington jet ($\dot{E}_w$). Here, all energies are normalized with the initial gravitational potential energy ($E_{p,0}$) and the time-derivative of energy with respect to dimensionless time is expressed as $\dot{E} = dE/d\hat{t}$. The
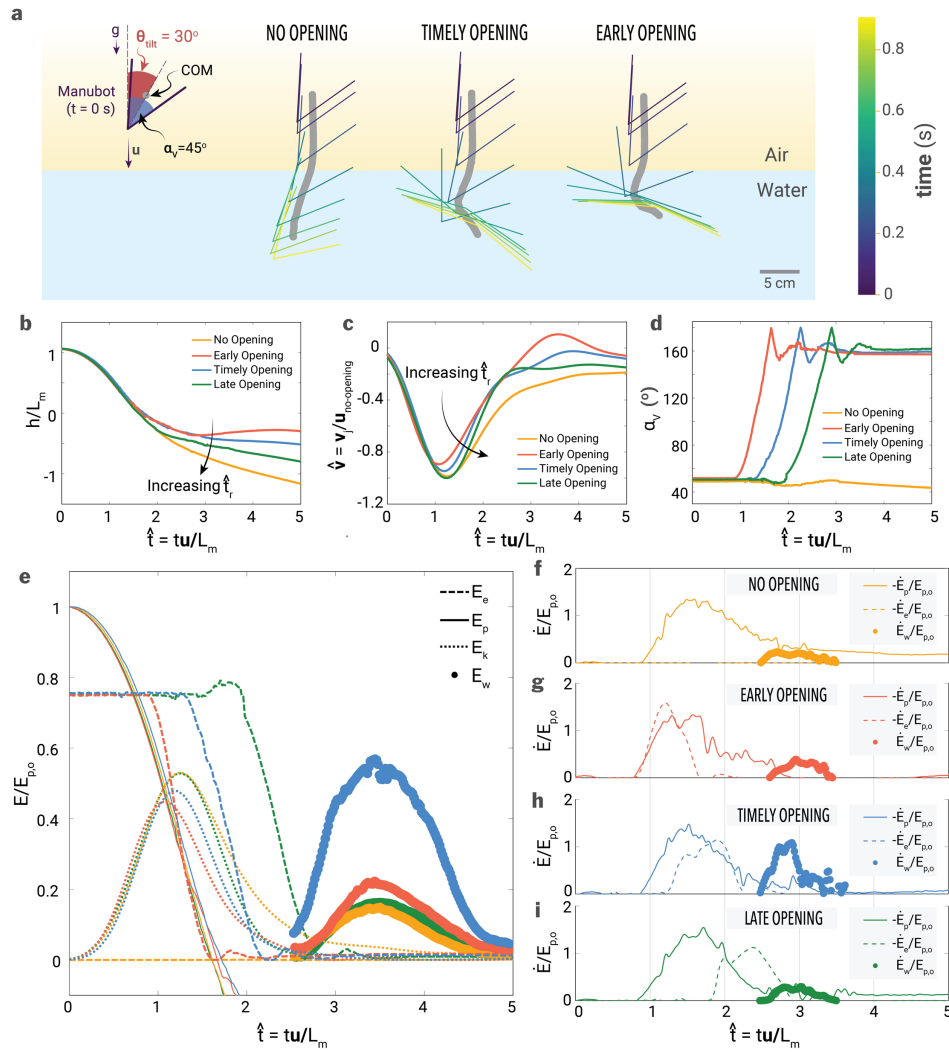
Figure 8. Kinematics and energy distribution of Manubot during water entry. (a) Trajectory of the Manubot and its centre of mass (COM) for scenarios with no body opening, early body opening and late body opening inside water. The Manubot is released from the air with an initial tilt angle of 30°. (b) Vertical position (h), normalized by the Manubot length (L_m). (c) Vertical velocity (u), normalized by the impact speed in the no-opening case (v_{impact}). (d) Body angle. (e) Energy distribution of gravitational potential energy (E_p), elastic potential energy (E_e), translational kinetic energy of the Manubot (E_k), and gravitational potential energy of the water column (E_w) for (e) early, (f) timely, and (g) late opening cases. (f–i) Flux of mechanical ($\dot{E}_p + \dot{E}_k$), elastic ($\dot{E}_e$) and jet potential energy ($\dot{E}_w$) for no-, early, timely, and late opening cases, respectively. Here, four representative cases are shown for $\hat{t}_r = 0.9$ (early opening), 1.3 (timely opening), 1.8 (late opening), and ∞ (no opening). All energies and fluxes are normalized by the initial gravitational potential energy ($E_{p,0}$).

fluxes of mechanical and elastic energy are shown in negative signs since they always decrease in this system. For all cases, the mechanical energy flux (($\dot{E}_k + \dot{E}_p$)/$E_{p,0}$, see solid line in figure 8f–i) emerges from the moment of water contact ($\hat{t} = 1$) and peaks at $\hat{t} = 1.5$–1.8 at which the centre of mass passes the surface level ($h = 0$). For the no-opening case (figure 8f), the mechanical energy flux gradually decreases from its maximum and saturates to a non-zero value because the Manubot keeps descending underwater due to its low hydrodynamic drag. On the other hand, for all dynamic cases in figure 8g–i, the flux of the mechanical energy vanishes at $\hat{t} \simeq 3$, indicating that the body opening can localize the transfer of mechanical energy to water flow within the short time range of $1 < \hat{t} < 3$ by increasing the hydrodynamic drag. Regardless of the body opening, the jet potential flux ($\dot{E}_w/E_{p,0}$) begins at a similar time ($\hat{t} \approx 2.5$), indicating that the energy transfer from the robot to the air cavity must be completed at least ($\hat{t} < 2.5$). By observation, when the Manubot opens its body too early ($\hat{t}_r < 1.1$), two separated air cavities are generated, weakening the Worthington jet (see figure 6f at $\hat{t} = 2.7$ and 4.0). This suggests the lower limit of $\hat{t}_r$ as 1.1. Since the time duration where $\dot{E}_w/E_{p,0} > 0$ is typically $\Delta\hat{t} = 1$ (figure 8f–i), the body opening time for enhancing the splash size should be within $1.1 < \hat{t}_r < 1.5$, which enables two potential energies (i.e. mechanical and elastic energy) released before the Worthington jet emerges. This aligns well with the observation in figure 8h where $\hat{t}_r = 1.3$. On the other hand, the Worthington jet's already develops when the supply of the jet potential energy flux is being fed for the late opening cases, which proves this case does not enhance the splash size. Therefore, the 'perfect' Manu jump (i.e. large Worthington splash generation) requires subtle control of body opening ($1.1 < \hat{t}_r < 1.5$) which enables the successive release of mechanical and elastic energy, which can deepen the pinch-off depth and result in a powerful water jet.

4. Conclusions

Our work provides a comprehensive understanding of the fluid dynamics of Manu jumping by integrating human data, controlled release experiments with solid V-shape projectiles, and the dynamic Manubot. We show that the size of the Worthington jets or splashes is governed by two key parameters: the V-angle and the timing of underwater body opening. These factors directly affect the dynamics of air cavity formation, pinch-off, and the resulting Worthington splash.

Human Manu jumping involves strategic aerial and underwater manoeuvres to increase air cavity size while minimizing impact forces on the body. Our analysis of 50 Manu jumping videos showed that the median V-angle during water entry was approximately 46.36°, closely aligning with the V-angle for solid projectiles to create the largest Worthington splashes. To the best of our knowledge, this is the first study to investigate the cavity and splash dynamics associated with the water entry of humans and their physical models, aimed at creating large splashes. Our experiments used V-shaped projectiles, which more accurately represent the human body compared with traditional spherical or cylindrical models.

To ensure the applicability of solid projectiles and Manubot experiments to human Manu jumping, these shapes were designed to replicate the human aspect ratio ($AR = 1 : 4$) and operate within a similar Froude number range ($1 < Fr < 100$). This range reflects a regime where inertial forces dominate over gravitational forces. Although the Bond number of the solid objects differs from that of humans by an order of magnitude, it remains $Bo \gg 1$, indicating that gravitational forces still dominate over surface tension. This difference arises due to the smaller characteristic length of the solid objects, a limitation of laboratory-scale experiments.

In the $Fr-Bo$ plot (figure 2c), humans, solid projectiles, and Manubot experiments all fall within the deep-seal regime ($1 < Fr < 100$, $10 < Bo < 10^5$). Within this regime, increasing the jumping height or impact speed of solid V-projectiles enhanced the splash size, similar to human Manu jumpers. Additionally, the Manubot effectively captured the qualitative splash dynamics of human Manu jumps by controlling the underwater body opening time.

Our experiments demonstrate that V-shaped projectiles, particularly at 45° angles, generate the fastest, tallest, and biggest Worthington jets at higher impact speeds, emphasizing the role of cavity pinch-off depth and shape in splash generation. This supports the use of a V-angle and a median angle of approximately 46° in human Manu jumps.

Our work on the dynamic Manubot highlights the role of underwater body opening in altering the splash dynamics. The precise timing of body opening enhances the cavity depth and delays pinch-off, leading to large Worthington splashes. Moreover, the splashes generated by the Manubot mimic the asymmetric splashes in Manu jumping, which occurs due to the asymmetric underwater body opening and non-zero tilt angles during water entry. Through energy analysis, the synchronization between the potential and kinetic energy transfer of Manubot is crucial during cavity formation of the largest splashes.

5. Broader implications and future directions

Our work offers broader implications for fluid dynamics, with potential applications in naval engineering, biomechanics, and systems influenced by factors such as body elasticity, surface wettability, and environmental conditions. Additionally, this work lays the groundwork for further explorations of water entry and underwater opening dynamics in generating the Worthington splash through the measurement of impact force profiles for solid projectiles, the Manubot, and human Manu jumpers. By using the Manubot and solid V-shaped projectiles, we approximated human dimensions through aspect ratios; however, future research should address projectile weight effects, an important factor in Manu jumping sports. Incorporating the anatomical complexity of human bodies into future experiments would further refine our understanding of splash dynamics. For our analysis of human Manu jumping data, we leveraged publicly available YouTube videos, which provide valuable semi-quantitative observational data. These efforts could be complemented in the future by high-precision experiments featuring divers equipped with body sensors, digital tracking markers, and high-speed imaging to simultaneously capture splash dynamics above and below the water.

Overall, our study explains the physics behind the 45° V-angle in Manu jumping and highlights how controlling underwater cavity dynamics drives big splashes, with implications for recreation and competitive water sports.

Appendix A. Manubot experimental setup

Figure 9 shows the experimental setup used to study Worthington jets generated by a Manubot. The release timing of the Manubot's two edges from the electromagnet was controlled using DC power and relays via an Arduino microprocessor, powered and programmed through a computer.
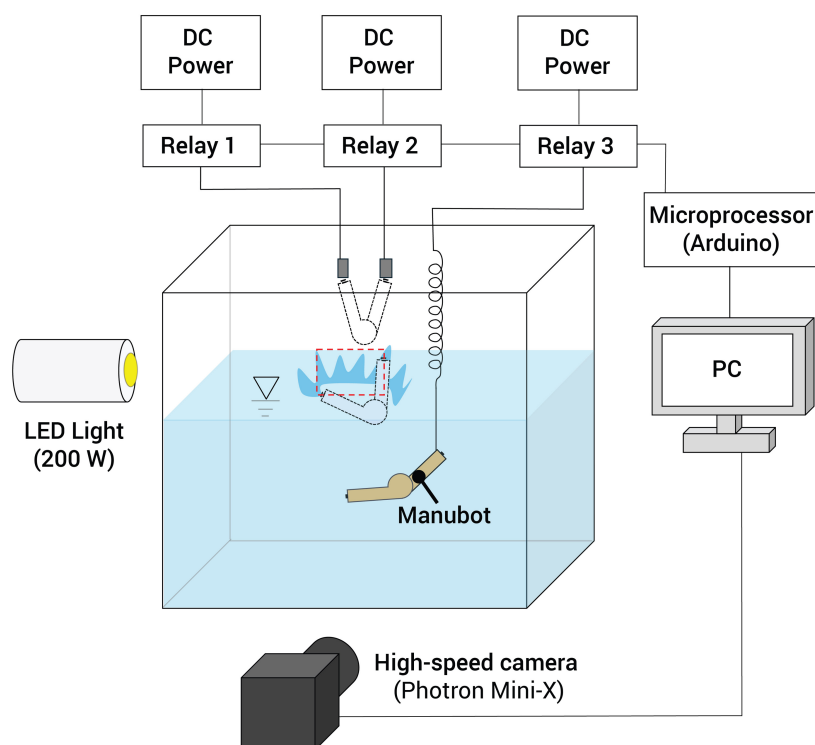

Figure 9. Experimental setup for studying splash dynamics of Manubot's water entry for varying release time, opening time and impact angles.

Appendix B. Temporal trajectory of vertical water entry of a flat projectile

Figure 10 shows the centre of the flat-shaped mass trajectories that enter the water at different impact speeds (figure 5b).
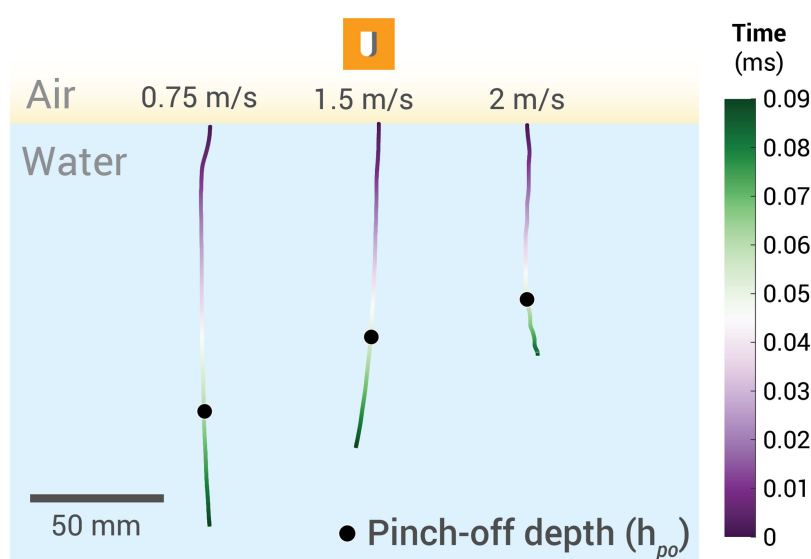

Figure 10. Temporal trajectories of the flat solid projectile ($\alpha_v = 0°$).

References

1. Manu Z. 2024 Z Manu world champs. See https://manuworldchamps.com/.
2. O'Neill Z. 2023 Pop some manus, diving in New Zealand with Zico O'Neill. See https://athletamag.com/en/pop-some-manus-diving-new-zealand-zico-oneill/.
3. Worthington AM. 1908 *A study of splashes*. London, UK: Longmans, Green, Company.
4. Gekle S, Gordillo JM. 2010 Generation and breakup of Worthington jets after cavity collapse. Part 1. Jet formation. *J. Fluid Mech.* **663**, 293–330. (doi:10.1017/s0022112010003526)
5. Truscott TT, Epps BP, Belden J. 2014 Water entry of projectiles. *Annu. Rev. Fluid Mech.* **46**, 355–378. (doi:10.1146/annurev-fluid-011212-140753)
6. Kim N, Park H. 2019 Water entry of rounded cylindrical bodies with different aspect ratios and surface conditions. *J. Fluid Mech.* **863**, 757–788. (doi:10.1017/jfm.2018.1026)
7. Guleria SD, Dhar A, Patil DV. 2021 Experimental insights on the water entry of hydrophobic sphere. *Phys. Fluids* **33**, 102109. (doi:10.1063/5.0063040)
8. Gekle S, Gordillo JM, van der Meer D, Lohse D. 2009 High-speed jet formation after solid object impact. *Phys. Rev. Lett.* **102**, 034502. (doi:10.1103/physrevlett.102.034502)
9. Okawa T, Kawai K, Kubo K, Kitabayashi S. 2022 Fundamental characteristics of secondary drops produced by early splash during single-drop impingement onto a thick liquid film. *Exp. Therm. Fluid Sci.* **131**, 110533. (doi:10.1016/j.expthermflusci.2021.110533)
10. Okawa T, Shiraishi T, Mori T. 2006 Production of secondary drops during the single water drop impact onto a plane water surface. *Exp. Fluids* **41**, 965–974. (doi:10.1007/s00348-006-0214-x)
11. Wagner H. 1932 Über Stoß- und Gleitvorgänge an der Oberfläche von Flüssigkeiten. *ZAMM J. Appl. Math. Mech. / Z. Für Angew. Math. Und Mech.* **12**, 193–215. (doi:10.1002/zamm.19320120402)
12. von Karman T. 1929 *The impact of seaplane floats during landing*. NASA Technical Report no. NACA TN 321.
13. Jamali M, Rostamijavanani A, Nouri NM, Navidbakhsh M. 2020 An experimental study of cavity and Worthington jet formations caused by a falling sphere into an oil film on water. *Appl. Ocean Res.* **102**, 102319. (doi:10.1016/j.apor.2020.102319)
14. Antolik JT, Belden JL, Speirs NB, Harris DM. 2023 Slamming forces during water entry of a simple harmonic oscillator. *J. Fluid Mech.* **974**, A23. (doi:10.1017/jfm.2023.820)
15. Jain U, Novaković V, Bogaert H, van der Meer D. 2022 On wedge-slamming pressures. *J. Fluid Mech.* **934**, A27. (doi:10.1017/jfm.2021.1129)
16. Fudge BD, Cimpeanu R, Antkowiak A, Castrejón-Pita JR, Castrejón-Pita AA. 2023 Drop splashing after impact onto immiscible pools of different viscosities. *J. Colloid Interface Sci.* **641**, 585–594. (doi:10.1016/j.jcis.2023.03.040)
17. Gordillo JM, Blanco-Rodríguez FJ. 2023 Theory of the jets ejected after the inertial collapse of cavities with applications to bubble bursting jets. *Phys. Rev. Fluids* **8**, 073606. (doi:10.1103/physrevfluids.8.073606)
18. Pegg M, Purvis R, Korobkin A. 2018 Droplet impact onto an elastic plate: a new mechanism for splashing. *J. Fluid Mech.* **839**, 561–593. (doi:10.1017/jfm.2018.60)
19. Negus MJ, Moore MR, Oliver JM, Cimpeanu R. 2021 Droplet impact onto a spring-supported plate: analysis and simulations. *J. Eng. Math.* **128**, 3. (doi:10.1007/s10665-021-10107-5)
20. Korkmaz FC, Güzel B. 2017 Water entry of cylinders and spheres under hydrophobic effects; case for advancing deadrise angles. *Ocean Eng.* **129**, 240–252. (doi:10.1016/j.oceaneng.2016.11.021)
21. Barjasteh M, Zeraatgar H, Javaherian MJ. 2016 An experimental study on water entry of asymmetric wedges. *Appl. Ocean Res.* **58**, 292–304. (doi:10.1016/j.apor.2016.04.013)
22. Vincent L, Xiao T, Yohann D, Jung S, Kanso E. 2018 Dynamics of water entry. *J. Fluid Mech.* **846**, 508–535. (doi:10.1017/jfm.2018.273)
23. Pandey A, Yuk J, Chang B, Fish FE, Jung S. 2022 Slamming dynamics of diving and its implications for diving-related injuries. *Sci. Adv.* **8**, eabo5888. (doi:10.1126/sciadv.abo5888)
24. Chang B, Croson M, Straker L, Gart S, Dove C, Gerwin J, Jung S. 2016 How seabirds plunge-dive without injuries. *Proc. Natl Acad. Sci. USA* **113**, 12006–12011. (doi:10.1073/pnas.1608628113)
25. Gregorio E, Balaras E, Leftwich MC. 2023 Air cavity deformation by single jointed diver model entry bodies. *Exp. Fluids* **64**, 168. (doi:10.1007/s00348-023-03712-w)
26. Brown JG, Abraham LD, Bertin JJ. 1984 Descriptive analysis of the rip entry in competitive diving. *Res. Q. Exerc. Sport* **55**, 93–102. (doi:10.1080/02701367.1984.10608383)
27. Lenz A, Provance B, Provance A. 2024 Making a splash: a closer look at early specialization in competitive diving. *Curr. Sports Med. Rep.* **23**, 376–380. (doi:10.1249/jsr.0000000000001206)
28. Delaloye JR, Sander F, Murar J, Tischer T, Ernstbrunner L. 2020 Water jumping sports. In *Injury and health risk management in sports: a guide to decision making* (eds W Krutsch, HO Mayr, V Musahl, F Della Villa, PM Tscholl, H Jones), pp. 651–657. Berlin, Germany: Springer. (doi:10.1007/978-3-662-60752-7_98)
29. Currie BM, Drew MK, Hetherington M, Waddington G, Brown NAT, Toohey LA. 2025 Diving into the health problems of competitive divers: a systematic review of injuries and illnesses in pre-elite and elite diving athletes. *Sports Health* **17**, 594–602. (doi:10.1177/19417381241255329)
30. Belilos E, Jow S, Maxwell M. 2023 Descriptive epidemiology of high school swimming and diving injuries. *Clin. J. Sport Med.* **33**, 428–434. (doi:10.1097/jsm.0000000000001121)
31. Glasheen JW, McMahon TA. 1996 Vertical water entry of disks at low Froude numbers. *Phys. Fluids* **8**, 2078–2083. (doi:10.1063/1.869010)
32. Aristoff JM, Bush JWM. 2009 Water entry of small hydrophobic spheres. *J. Fluid Mech.* **619**, 45–78. (doi:10.1017/s0022112008004382)
33. Gekle S, van der Bos A, Bergmann R, van der Meer D, Lohse D. 2008 Noncontinuous Froude number scaling for the closure depth of a cylindrical cavity. *Phys. Rev. Lett.* **100**, 084502. (doi:10.1103/physrevlett.100.084502)
34. May A. 1952 Vertical entry of missiles into water. *J. Appl. Phys.* **23**, 1362–1372. (doi:10.1063/1.1702076)
35. Birkhoff G, Isaacs R. 1951 Transient cavities in air–water entry. *Navord Rep.* **1490**, 68–72.
36. Choi D, Byun J, Park H. 2022 Analysis of liquid column atomization by annular dual-nozzle gas jet flow. *J. Fluid Mech.* **943**, A25. (doi:10.1017/jfm.2022.435)
37. Rohilla P, Choi D, Wallace HJ, Yung KL, Deora J, Lele A, Bhamla S. 2025 Mastering the Manu—how humans create large splashes. Zenodo. (doi:10.5281/zenodo.14984672)
38. Rohilla P, Choi D, Wallace H, Yung KL, Deora J, Lele A *et al*. 2025 Supplementary material from: Mastering the Manu—how humans create large splashes. Figshare. (doi:10.6084/m9.figshare.c.7735222)